Optics Letters

Distinguishing optical and acoustic phonon temperatures of supported 2D materials by nanosecond time-resolved Raman scattering

Mahya Rahbar,[1] Ibrahim Al Keyyam,[1] Jing Liu,[2] and Xinwei Wang[1,*]

[1]Department of Mechanical Engineering, Iowa State University, Ames, Iowa 50011, USA
[2]College of New Materials and New Energies, Shenzhen Technology University, Shenzhen, Guangdong 518118, China
*xwang3@iastate.edu

Received 19 June 2024; revised 13 August 2024; accepted 13 August 2024; posted 15 August 2024; published 28 August 2024

Upon laser irradiation, 2D materials experience a cascading energy transfer from electrons to optical phonons (OPs) and then to acoustic phonons (APs), resulting in a significant thermal non-equilibrium among energy carriers. This non-equilibrium presents challenges for Raman-based thermal characterization, as Raman scattering measures only OP temperature rise, while APs are the primary energy carriers. Despite recent efforts to address this issue, OP–AP thermal non-equilibrium in supported 2D materials remains poorly resolved. Here, we develop a method to distinguish the OP and AP temperature rises based on their different temporal thermal responses under laser irradiation: the OP–AP temperature difference responds almost immediately (~a few to tens of ps), while the AP temperature rise takes longer to establish (~tens of ns). Using energy transport-state resolved Raman, we probe the transient thermal response of Si-supported nm-thick MoS_2 from 20 to 100 ns. We find that the OP–AP temperature difference exceeds 120% of the AP temperature rise under ~0.439 μm radius laser heating. The intrinsic interfacial thermal conductance of the samples, based on the true AP temperature rise, varies from 0.199 to 1.46 $MW{\cdot}m^{-2}{\cdot}K^{-1}$, showing an increasing trend with sample thickness.

https://doi.org/10.1364/OL.532999

Due to their unique optical, thermal, mechanical, and electrical properties [1–4], two-dimensional (2D) materials, such as transition-metal dichalcogenides (TMDs) and graphene, have garnered significant interest in various fields [5,6]. Understanding the thermal transport characteristics of these materials is crucial for designing advanced devices. Raman spectroscopy is a widely used technique for measuring these properties; however, it typically assumes thermal equilibrium between optical phonons (OPs) and acoustic phonons (APs) despite significant non-equilibrium caused by laser irradiation and the cascading energy transfer from electrons to OPs and then to APs. Ignoring this temperature difference can lead to considerable deviations in the measured thermal properties, as APs are the primary energy carriers, while Raman scattering primarily measures OP temperature. Our research group has extensively addressed this issue for both supported and suspended 2D materials [7–10]. Nonetheless, distinguishing between OP and AP temperature rises remains a significant challenge, especially for supported 2D materials where in-plane heat conduction, hot carrier diffusion, and interface thermal resistance (ITR) complicate the situation.

Here, a method is developed based on the nanosecond time-resolved energy transport-state resolved Raman (nanosecond time-resolved ET-Raman) to distinguish the OP–AP thermal nonequilibrium of supported 2D materials. This technique is based on the different temporal responses of OP and AP temperatures upon laser heating: the OP–AP temperature difference (ΔT_{OA}) exhibits nearly instantaneous temporal response (~a few to tens of ps), whereas the AP temperature rise (ΔT_{AP}) is governed by heat conduction, taking tens of nanoseconds or longer to establish. The intrinsic ITR between nm-thick MoS_2 and Si substrate is also determined based on the true AP temperature response.

In supported 2D materials, the AP–OP energy cascading occurs due to photon irradiation, as further explained in Supplement 1. Therefore, assessing the temperature rise in these materials during photoexcitation requires specialized considerations. This study employs the nanosecond time-resolved ET-Raman technique with a 532 nm CW laser, as shown in Figs. 1(a) and 1(b). It is important to highlight that the Raman light provides insight into the temperature of OPs [7]. To measure the OP temperature rise using the nanosecond time-resolved ET-Raman technique, two distinct energy transport states, continuous wave (CW) laser and amplitude-modulated CW laser, are used. The amplitude-modulated CW laser is the CW laser modulated to a square-waveform under different frequencies. This frequency is adjusted such that the duration of the laser-off time (t_{off}) remains fixed at 500 ns, while the duration of the laser-on time (t_{on}) varies from 20, 40, 60, 80 to 100 ns. The t_{off} duration allows the sample to cool completely before the next laser pulse. As a result of laser irradiation, the sample's AP temperature rises. Since the laser energy is transferred from OPs to APs, there is also an OP temperature rise over that of APs. Raman scattering measures this OP temperature rise, which is higher than that of APs. Consequently, the effect of AP temperature rise in the measured thermal response increases

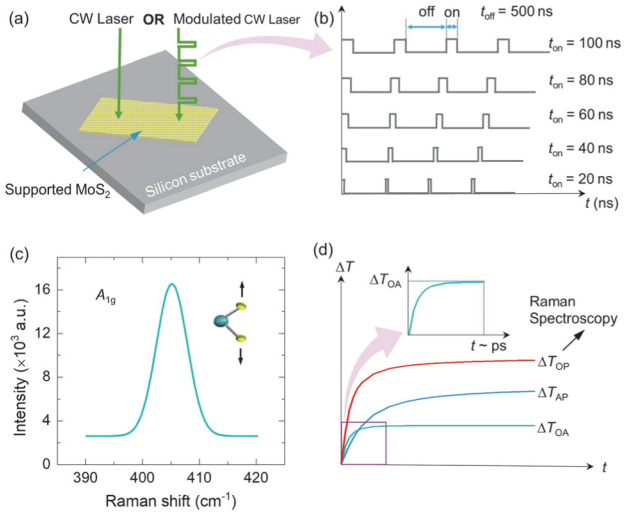

Fig. 1. The physical principle of nanoscale time-resolved ET-Raman. (a) nm-thick MoS_2 sample on the Si substrate being irradiated by CW or amplitude-modulated laser. (b) Amplitude-modulated CW laser heating with different laser-on time (t_{on}= 20, 40, 60, 80, 100 ns) and fixed laser-off time (t_{off} = 500 ns). (c) Raman spectrum corresponding to the A_{1g} mode of MoS_2 used in this study. (d) Schematic of the temperature rise of OP, AP, and the OP–AP temperature difference versus time (not to scale). ΔT_{OA} rapidly reaches the steady state (~few to tens of ps) while ΔT_{AP} takes a longer time (~tens of ns).

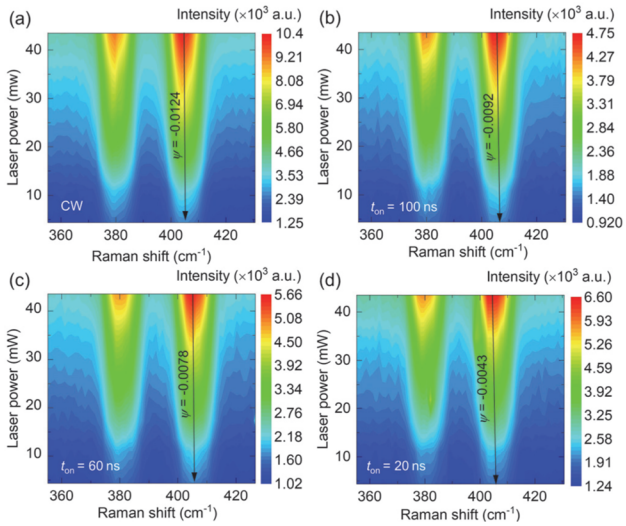

Fig. 2. Measured ψ of the A_{1g} mode of MoS_2 under 20× objective lens for location 1 of sample 1 under (a) CW laser, amplitude-modulated CW laser state with (b) t_{on} = 100 ns, (c) t_{on} = 60 ns, and (d) t_{on} = 20 ns.

with the increased t_{on} (the CW case has the highest temperature rise). As t_{on} approaches zero (using extrapolation), the observed thermal response predominantly reflects the effect of OP–AP temperature difference, which establishes in a very short time. Figure 1(d) shows the schematic of the temperature rise of OPs, APs, and the OP–AP temperature difference over time. They follow this relation $\Delta T_{OP} = \Delta T_{AP} + \Delta T_{OA}$. ΔT_{OA} increases and reaches to steady state within picoseconds, which is much faster than ΔT_{AP}. This implies that even as the time approaches zero ns, the ΔT_{OA} persists.

The OP temperature rise within a small range of laser power (e.g., 4.35 to 43.5 mW for the 20× lens) is linearly proportional to the laser intensity (I). This relationship is demonstrated by the Raman shift power coefficient (RSC), denoted by ψ ($\psi = \partial\omega/\partial P$). In this work, three different objective lenses (20×, 50×, and 100×) are employed to differentiate the laser-heated area. Due to the higher energy density under a more focused laser beam, we expect $|\psi_{CW,\,20\times}| < |\psi_{CW,\,50\times}| < |\psi_{CW,\,100\times}|$. Physics regarding the use of different laser heating sizes is provided later. A deeper understanding of the nanosecond time-resolved ET-Raman technique can be found in previously published works [11,12]. Due to the relatively weak intensity and higher uncertainty of the in-plane E_{2g} mode of MoS_2 (at 381 cm^{-1}) than the out-of-plane A_{1g} mode (at 406 cm^{-1}), the A_{1g} mode is used for data analysis, as shown in Fig. 1(c). Note that the ψ values are determined using the cross correlation method [13] as explained in Supplement 1. This study uses two MoS_2 samples with thicknesses of 25 and 10 nm, as revealed by atomic force microscopy and detailed in Supplement 1.

Figure 2 shows the 2D contours of the measured Raman spectra under different laser powers, illustrating the linearity of the Raman redshift with laser power. The shown conditions include CW laser and amplitude-modulated CW laser with t_{on} of 100, 60, and 20 ns, as examples. These measurements are conducted under a 20× objective lens at location 1 of sample 1. It can be seen that $|\psi|$ decreases as t_{on} decreases. During the laser-on time, the sample's temperature rises due to laser heating, and Raman scattering is excited and collected. During the laser-off time, the sample cools as heat dissipates to the Si substrate, and Raman scattering is not excited or collected. Therefore, $|\psi|$ demonstrates a decreasing tendency with decreased t_{on}.

Figures 3(a), 3(c), and 3(e) shows the $\psi_{ns} \sim t_{on}$ curves for all cases using three objective lenses, aiming to identify a relationship between these parameters. Note that the measured ψ_{ns} has contributions of ΔT_{OA} (ψ_{OA}) and ΔT_{AP} (ψ_{AP}) as $\psi_{ns} = \psi_{AP} + \psi_{OA}$. It is found the $\psi_{ns} \sim t_{on}$ relation can be fitted very well with a second-order polynomial function, and ψ_{OA} can be readily determined. More discussions about the determined ψ_{OA} will be given later. Beyond this, we also introduce, to our knowledge, a novel fitting model to fit the data, facilitating subsequent determination of ψ_{OA}. Furthermore, it can be seen that for each sample, $|\psi_{ns}|$ decreases as t_{on} decreases.

The ψ value obtained from the nanosecond time-resolved ET-Raman reflects the temperature rise of OPs. However, the main energy carriers are APs. Thus, we subtract ΔT_{OA} from the measured OP temperature rise and normalize ψ_{ns} as $\psi_{AP,N} = (\psi_{ns} - \psi_{OA})/(\psi_{CW} - \psi_{OA})$. Employing the lumped method, the energy transport equation of the sample is expressed as follows:

$$Q'' - G \cdot \Delta T = \rho c_p \Delta z \frac{\partial \Delta T}{\partial t}, \quad (1)$$

where Q'' is the constant surface laser heating per unit area, G is the interfacial thermal conductance (ITC) per unit area, ρ is the density, cp is the specific heat, and Δz is the sample thickness. Note that the temperature rise of the Si substrate is negligible due to its very high thermal conductivity. Furthermore, due to the very small size of the sample and its high thermal conductivity, the Biot number, representing the ratio of internal resistance (conduction) to external resistance (convection plus conduction), is extremely small in our case. Consequently, the lumped method is applicable here. Here, G

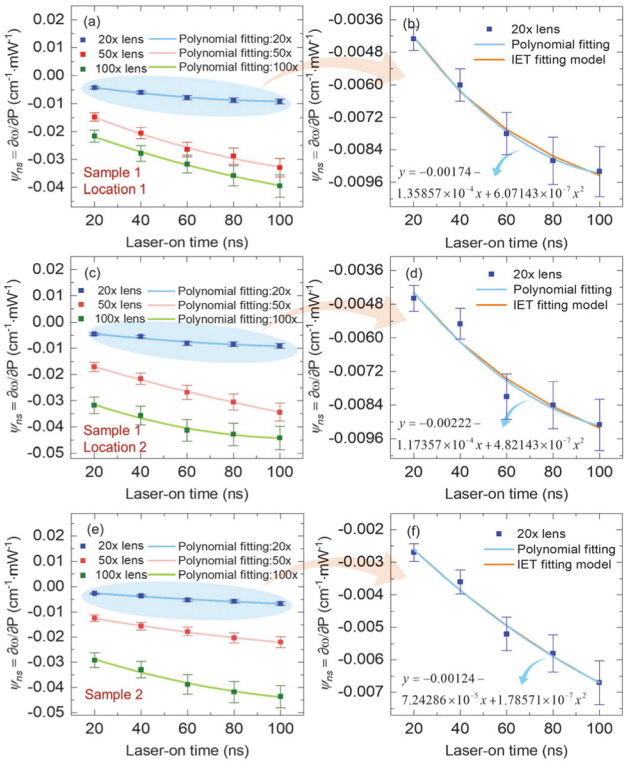

Fig. 3. The second-order polynomial fitted ψ data for three objective lenses using the amplitude-modulated CW laser for (a) location 1 of sample 1, (c) location 2 of sample 1, and (e) sample 2. Magnified data obtained with the 20× objective lens along with the second-order polynomial and IET fitting model for (b) location 1 of sample 1, (d) location 2 of sample 1, and (f) sample 2. Error bars show the upper bound of uncertainty in our measurements.

incorporates the effects of in-plane heat conduction and hot carrier diffusion, whose effect will be negligible when the laser spot size (r_0) is large (e.g., 20×). The temperature rise of the sample is solved as $\Delta T = \Delta T_0[1 - exp(-t/\tau)]$, where $\Delta T_0 = Q''/G$ and $\tau = \rho c_p \Delta z/G$. The normalized average of the sample's temperature response over the heating period can be readily derived as $\Delta T^* = \Delta T/\Delta T_0 = 1 - \tau/t[1 - exp(-t/\tau)]$. Then, comparing the theoretical normalized temperature rise of the sample with the experimental normalized AP temperature rise, the experimental ψ_{ns} can be expressed as $\psi_{ns} = [1 - \tau/t(1 - exp(-t/\tau))] \cdot \psi_{AP} + \psi_{OA}$, which serves as a new fitting model termed "interfacial energy transfer" (IET) model for fitting the experimental ψ_{ns}. Both fittings, utilizing the second-order polynomial and IET models, are shown in Figs. 3(b), 3(d), and 3(f) for all three cases under the 20× objective lens. As observed, the IET model aligns closely with the data and exhibits good agreement with the polynomial fitting. By considering t_{on} limit of zero, ψ_{OA} can be determined in both models. It is important to note that the IET model is not applicable to 50× and 100× cases due to the non-negligible effects of the in-plane heat conduction and hot carrier diffusion associated with their smaller laser spot sizes. More information can be found in Supplement 1.

By fitting the experimental data (ψ_{ns}) with the IET model, three parameters, including ψ_{AP}, ψ_{OA}, and τ, and subsequently the intrinsic ITC (G) between MoS_2 and Si substrate are determined. The results are summarized in Table 1. Note that the ψ_{OA} values obtained from the IET model closely resemble the values

Table 1. Direct Measurement of ψ_{AP} and ψ_{OA} and Intrinsic Interfacial Thermal Conductance for the A_{1g} Mode of MoS_2 Using the 20× Objective

Sample #	Thickness [nm]	ψ_{AP} [$cm^{-1}\cdot mW^{-1}$]	ψ_{OA} [$cm^{-1}\cdot mW^{-1}$]	G [$MW\cdot m^{-2}\cdot K^{-1}$]
Sample 1, Location 1	25	−0.0117	−0.00127	1.46
Sample 1, Location 2	25	−0.0117	−0.00207	1.10
Sample 2	10	−0.0144	−0.00120	0.199

obtained from the second-order polynomial fitting, which are −0.00174, −0.00222, and −0.00124 $cm^{-1}\cdot mW^{-1}$ for locations 1 and 2 of sample 1, and sample 2, respectively.

One noticeable observation is that ITC (G, inverse of ITR) is smaller for the thinner sample. During mechanical exfoliation, wrinkles and defects are likely to form, especially in thinner samples. As shown in Figs. S1(c) and S1(d), the thinner sample (#2) exhibits more surface roughness, while the thicker sample (#1) appears smoother. These wrinkles and defects decrease the ITC. Yuan *et al.* [14] also confirmed that 2D materials, particularly thinner samples, are prone to folding and wrinkle formation during mechanical exfoliation, reducing ITC. They reported an increase in G with an increased layer number of the supported MoS_2 on the Si substrate at room temperature, with G values of 0.974 $MW\cdot m^{-2}\cdot K^{-1}$ for a 4.2 nm MoS_2 and 68.6 $MW\cdot m^{-2}\cdot K^{-1}$ for a 45 nm MoS_2 sample. Taube *et al.* [15] measured the G of the monolayer MoS_2 supported on the SiO_2/Si substrate to be 1.94 $MW\cdot m^{-2}\cdot K^{-1}$ at 300 K employing Raman spectroscopy. Yue *et al.* [16] reported the G of 5-layered MoS_2 on the SiO_2/Si substrate to be 1.73 $MW\cdot m^{-2}\cdot K^{-1}$ using Raman spectroscopy. Discrepancies between literature findings and our results are partially due to variations in surface structure and experimental uncertainty. Furthermore, the previously reported G using Raman spectroscopy did not rule out the thermal nonequilibrium between OPs and APs. Also, the large errors in laser absorption calculation will cause considerable uncertainties in those works. Moreover, the G values reported in literatures correspond to 2D samples of varying thicknesses, which limit their direct comparability to our results. Note that the G calculation in our study includes a 15% uncertainty, which is primarily due to uncertainties in the Raman signal and can be reduced with better-controlled experimental conditions.

For the three measured cases, the ψ_{OA} and its ratio to the ψ_{AP} are presented in Fig. 4. As shown in Fig. 4(a), there is a decreasing trend for $|\psi_{OA}|$ versus increased laser spot size. This trend

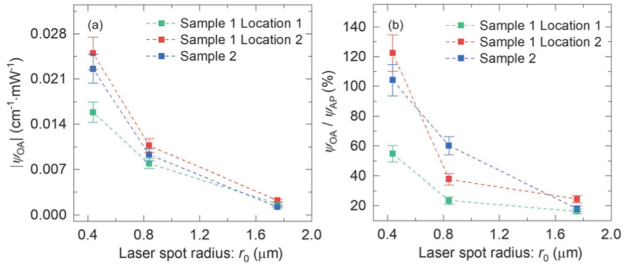

Fig. 4. (a) Plots showing the ψ_{OA} and (b) contribution of ψ_{OA} to the ψ_{AP} against laser spot size, obtained from the second-order polynomial fitting. Error bars show the upper bound of uncertainty analysis for measurements.

highlights the stronger thermal non-equilibrium between phonon branches under smaller heating areas (using 100× objective). Note that these data are obtained from the second-order polynomial fitting since the IET model is not applicable for 50× and 100× objective cases. For the laser spot size measurement, we use the Gaussian beam's radial distribution as $I = I_0 exp(-r^2/r_0^2)$. More details are available in Supplement 1.

The increasing trend of ψ_{OA} versus decreased laser spot size is consistent with the findings of Zobeiri *et al*. [9] for the supported MoS_2 on the quartz substrate. This suggests that the OP–AP non-equilibrium effect becomes more significant with reduced laser heating size due to the higher absorbed energy intensity per unit volume as the laser spot size decreases. When the total laser energy is constant, we have $\Delta T_{OA} \propto I \propto r_0^{-2}$. Figure 4(b) shows the variation of ψ_{OA}/ψ_{AP} against the laser spot size, displaying a decreasing trend. This is because ΔT_{AP} depends on both the laser spot size and sample's thermal conductivity, resulting in its dependency on r_0 as $\Delta T_{AP} \propto r_0^{-n}$ with $n < 2$. Therefore, ψ_{OA}/ψ_{AP} increases with the decreased laser spot size. This physical phenomenon has been thoroughly demonstrated in previous works conducted in our lab [8,17].

This work developed a ns time-resolved idea to directly characterize the thermal non-equilibrium between OPs and APs in the supported 2D materials. For the characterized $\psi_{ns} \sim t_{on}$ trend, a physical mode (IET for large laser spot size) and a mathematical model for general situations were developed to determine the contribution of ΔT_{OA} to ψ. It was found that the OP–AP thermal non-equilibrium effect becomes more important for decreased laser spot size. ψ_{OA}/ψ_{AP} reached >120% for a 25 nm-thick MoS_2 sample under 0.439 μm radius laser heating. It highlights the importance of thermal non-equilibrium effects in smaller heating areas, as ignoring them could cause significant errors in determining thermal properties. The interfacial thermal conductance between the nm-thick MoS_2 and the Si substrate, based on true AP temperature rise, was found to increase (0.199–1.46 $MW \cdot m^{-2} \cdot K^{-1}$) with sample thickness.

Funding. Shenzhen Scientific and Technological Foundation (JCYJ20220530153401003); National Natural Science Foundation of China (12204320); Basic and Applied Basic Research Foundation of Guangdong Province (2020A1515110389); U.S. National Science Foundation (2032464).

Disclosures. The authors declare no conflicts of interest.

Data availability. Data underlying the results presented in this paper are not publicly available at this time but may be obtained from the authors upon reasonable request.

Supplemental document. See Supplement 1 for supporting content.

REFERENCES

1. J. L. Pura, Crystals **13**, 108 (2023).
2. Q. H. Wang, K. Kalantar-Zadeh, A. Kis, *et al.*, Nat. Nanotechnol. **7**, 699 (2012).
3. A. Gupta, T. Sakthivel, and S. Seal, Prog. Mater. Sci. **73**, 44 (2015).
4. D. Akinwande, C. J. Brennan, J. S. Bunch, *et al.*, Extreme Mech. Lett. **13**, 42 (2017).
5. S. Kim, A. Konar, W.-S. Hwang, *et al.*, Nat. Commun. **3**, 1011 (2012).
6. K. Chang and W. Chen, ACS Nano **5**, 4720 (2011).
7. N. Hunter, N. Azam, H. Zobeiri, *et al.*, Adv. Mater. Interfaces **9**, 2102059 (2022).
8. R. Wang, H. Zobeiri, Y. Xie, *et al.*, Adv. Sci. **7**, 2000097 (2020).
9. H. Zobeiri, N. Hunter, N. Van Velson, *et al.*, Nano Energy **89**, 106364 (2021).
10. S. Xu, N. Hunter, H. Zobeiri, *et al.*, Mater. Today Phys. **27**, 100816 (2022).
11. R. Wang, N. Hunter, H. Zobeiri, *et al.*, Phys. Chem. Chem. Phys. **24**, 22390 (2022).
12. S. Xu, T. Wang, D. Hurley, *et al.*, Opt. Express **23**, 10040 (2015).
13. N. Hunter, M. Rahbar, R. Wang, *et al.*, Opt. Lett. **47**, 6357 (2022).
14. P. Yuan, C. Li, S. Xu, *et al.*, Acta Mater. **122**, 152 (2017).
15. A. Taube, J. Judek, A. Łapińska, *et al.*, ACS Appl. Mater. Interfaces **7**, 5061 (2015).
16. X. F. Yue, Y. Y. Wang, Y. Zhao, *et al.*, J. Appl. Phys. **127**, 104301 (2020).
17. H. Zobeiri, N. Hunter, R. Wang, *et al.*, Adv. Sci. **8**, 2004712 (2021).